applied sciences

MDPI

Article

A Model to Simulate Gas Dissolution into/through Metals and Its Application to Deuterium in a 316L Steel Chamber with Pb-Li in a Quasi-2D Geometry †

Tiago Pomella Lobo [1,2,*,‡], Ester Diaz-Alvarez [2] and Laëtitia Frances [2]

[1] Fusion Group, Department of Applied Physics, Eindhoven University of Technology (TU/e), 5612 AP Eindhoven, The Netherlands

[2] Tritium Laboratory Karlsruhe (TLK), Karlsruhe Institute of Technology (KIT), 76344 Eggenstein-Leopoldshafen, Germany; ester.diaz-alvarez@kit.edu (E.D.-A.); laetitia.frances@protonmail.com (L.F.)

* Correspondence: t.pomella-lobo@outlook.com or t.pomella-lobo@kit.edu

† This paper is an extended version of a Master thesis developed for the Eindhoven University of Technology (TU/e).

‡ Current address: Institute for Neutron Physics and Reactor Technology (INR), Karlsruhe Institute of Technology (KIT), 76344 Eggenstein-Leopoldshafen, Germany.

Abstract: Liquid lead-lithium in eutectic proportions (Pb-Li) is a candidate material for Breeding Blankets (BBs) in future Fusion Power Plants (FPP). BB design depends on the diffusivity and Sieverts' constant (solubility) of tritium in this alloy, but literature reports a large scattering of measurements for these values. A model was developed to address one possible source of this scattering in static experiments, i.e., non-negligible loss of hydrogen gas through steel walls of containers. This model simulates the dissolution of gases into, and their diffusion through, metallic barriers for diffusivity and Sieverts' constant as inputs. When implemented, it can be used to compute the pressure decrease in a metallic chamber, and comparison of simulated curves with experimental ones allows for estimates of the diffusivity and Sieverts' constant. This approach was used to estimate these coefficients for deuterium in stainless steel, using experiments performed with a 316L steel chamber from an existing facility (the Vacuum Sieve Tray setup) and simulations in a quasi-2D representation of this chamber. This validated the model, which was then used to simulate the chamber containing Pb-Li, as a means of planning for future experiments.

Keywords: Pb-Li; tritium; diffusivity; solubility; sieverts; permeation; breeding blanket; gas-metal interaction

check for updates

Citation: Pomella Lobo, T.; Diaz-Alvarez, E.; Frances, L. A Model to Simulate Gas Dissolution into/through Metals and Its Application to Deuterium in a 316L Steel Chamber with Pb-Li in a Quasi-2D Geometry. *Appl. Sci.* **2022**, *12*, 2523. https://doi.org/10.3390/app12052523

Academic Editor: Arkady Serikov

Received: 10 December 2021
Accepted: 20 February 2022
Published: 28 February 2022

1. Introduction

The European DEMOnstration Power Plant (EU-DEMO) is foreseen to consume more than 100 kg of tritium (T, or ${}^{3}_{1}$H) per full-power-year of operation [1]. Given its scarcity from natural and anthropogenic sources [2], tritium self-sufficiency is considered a strong requirement for future Fusion Power Plants (FPPs) [3]. That is, tritium must be produced in situ by Breeding Blanket (BB) systems, using a combination of Neutron Multiplier Material (NMM) and lithium compound (breeder). Liquid lead-lithium in eutectic proportions (herein referred to as Pb-Li) can act as both breeder and NMM, so it has been chosen for some BB concepts, including one of the current designs under Research and Development (R&D) focus, the Water-Cooled Liquid-Lithium (WCLL) concept [1].

Design of BB concepts is not only driven by tritium economy requirements, but also safety concerns. Design studies of both aspects must assess crucial mitigation strategies for permeation losses, since FPPs must comply with hard requirements on environmental releases and plant inventory due to retention [4,5]. Hydrogen permeation through metals is largely governed by its characteristic diffusivity and Sieverts' constant (solubility), but literature reports a rather large scattering of measurements for these values for Pb-Li, especially for the latter: over two and four orders of magnitude, respectively. The difference between higher and lower values can be decisive in the feasibility of FPPs, which warrants a reduction of this uncertainty [6].

Possible reasons for this uncertainty include experimental methodology and associated measurement techniques. In particular, static experiments attempt to infer the Sieverts' constant by measuring: (a) how much of a fixed initial amount of hydrogen is absorbed by a Pb-Li sample; or (b) how much hydrogen desorbs from a Pb-Li sample previously exposed to a hydrogen atmosphere [6,7]. In both cases, however, the eventual passage of hydrogen through the experimental container walls is non-negligible; walls are usually made of steel, which presents solubility, for the great majority of literature measurements, at least one order of magnitude higher than Pb-Li. This can interfere with the accuracy of measurements and lead to an overestimation of absorption or underestimation of desorption. Thus, it is crucial for any experiment of this type to distinguish the dissolution of gas into samples from the loss of gas through the container walls.

To tackle this, a physical model for gas dissolution into metals was developed (Sections 2 and 3). Subsequently, it was applied to part of an experimental setup, designed to study the Vacuum Sieve Tray (VST) concept for hydrogen extraction from Pb-Li, in the Tritium Laboratory Karlsruhe (TLK) [8]. The derived numerical model was used to estimate the diffusivity and Sieverts' constant for 316L steel in a control experiment without Pb-Li, and comparison with literature allowed for model validation (Section 4). The model was then applied to a simulated experiment with Pb-Li, to provide predictions and guidelines for future measurements with the setup (Section 5).

2. Background for Modelling Gas Dissolution into and through Metals

Figure 1 displays the expected process undergone by a diatomic gas when passing through a generic metal barrier. In this process, generally the gas phase dynamics (i) evolve much faster than the diffusion (iii) in the solid medium [9]. Thus:

- the gas can be always considered in equilibrium for the purpose of evaluating thermodynamic properties (pressure, density, ...) that affect the gas-metal interaction; and
- the diffusion is mainly determined by surface dynamics, and not gas availability outside of the metal.

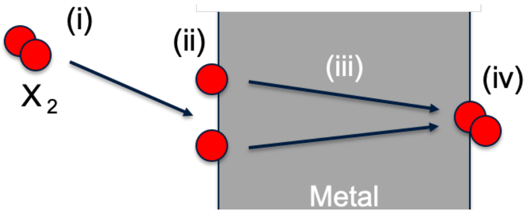

Figure 1. Diagram of the passage of a diatomic gas (X_2) through a generic metal barrier. The process is subdivided in four steps. (i) Free gas expansion, to reach the gas-metal interface (i.e., the metal surface). (ii) Adsorption + Dissociation, at the interface. (iii) Diffusion, through the metallic medium in the direction of lower concentrations. (iv) Recombination + Desorption, at the other gas-metal interface.

For any given gas-metal pair, the surface dynamics (ii and iv) characterize the process as either surface-controlled or bulk-controlled. In surface-controlled systems the gas intake rate through the interface limits the diffusion process, due to slow adsorption or chemical reactions. In bulk-controlled systems, the gas dissolution into the metal is only determined by the medium's diffusivity, because the concentration at the interface is high enough to supply the fluxes determined by the diffusive process [10]. It is generally agreed that hydrogen isotopes diffusion into Pb-Li and steel are bulk-controlled systems [10–14], although exceptions have been reported for Pb-Li [9].

The diffusion process (iii) has two distinct stages: a diffusive one, that is transient and lasts until medium saturation, and a permeative one, when in steady state—a system's steady-state flux is mathematically described by Richardson's Permeation Law [14]. For a metal M and a diatomic gas X_2 in low pressure regimes—a gas is considered in a low pressure regime, and thus the ideal gas law may be applied, when its reduced pressure is much smaller than 1, i.e., its pressure is far from its critical point [15,16]—both stages are governed by the diffusivity $\mathcal{D}_X^M$ ($\mathrm{m^2/s}$) and the Sieverts' constant $\mathcal{S}_{X_2}^M$ ($\mathrm{mol/m^3\sqrt{Pa}}$). This process can be mathematically described by Fick's Law—Equation (1)—and the principle of mass continuity—Equation (2)—which respectively relate: the gradient of the local concentration of a species to the molar flux of this species, and the divergence of such flux to the time variation of that concentration. Saturation profiles depend on the boundary conditions, which can be determined using Sieverts' Law—Equation (3).

$$\overrightarrow{Q_X} = -\mathcal{D}_X^M \cdot \overrightarrow{\nabla}\, c_X \tag{1}$$

$$\frac{\partial}{\partial t} c_X + \boldsymbol{\nabla} \bullet \left(\overrightarrow{Q_X}\right) = 0 \tag{2}$$

$$c_X^* = \mathcal{S}_{X_2}^M \cdot \sqrt{p_{X_2}} \tag{3}$$

In the equations, c_X ($\mathrm{mol/m^3}$) is the metal's concentration of atoms X and c_X^* is the Sieverts' equilibrium concentration; $\overrightarrow{Q_X}$ ($\mathrm{mol/m^2 s}$) is the molar flux of X; p_{X_2} (Pa) is the partial pressure of X_2 in the gas phase [14].

Dimensional analysis shows that the diffusivity displays physical unit of time, while the Sieverts' constant does not. This means a varying experimental quantity that represents the process, such as the pressure, can be used to measure:

- diffusivity, by verifying time-related properties of a pressure curve characterization;
- Sieverts' constant, by comparing initial and final states of a pressure curve characterization;

in a given static experiment [14].

Both $\mathcal{D}_X^M$ and $\mathcal{S}_{X_2}^M$ display an Arrhenius dependency to temperature T (K), as shown in Equations (4) and (5).

$$\mathcal{D} = D_\infty \cdot e^{-\frac{E_d}{\mathcal{R}\cdot T}} \tag{4}$$

$$\mathcal{S} = S_\infty \cdot e^{-\frac{E_s}{\mathcal{R}\cdot T}} \tag{5}$$

The terms E_d and E_s are referred to as *activation energies* ($\mathrm{J/mol}$). For the purposes of this work, the terms D_∞ and S_∞ will be called *infinite-temperature* coefficients. All four terms (D_∞, S_∞, E_d and E_s) will be addressed as *dissolution parameters*. For a given set of temperature-dependent measurements, the dissolution parameters can be obtained by linear regression of data plotted, in logarithmic scale, as function of the reciprocal of the temperature ($1/T$) [14].

Figure 2 shows a literature review of Arrhenius functions of diffusivity and Sieverts' constant for the dissolution of different hydrogen isotopes (Q) in Pb-Li. Notice the scattering over orders of magnitude, especially in Figure 2b. When only point measurements were available, the curves were interpolated (but not extrapolated) using logarithmic regression. Sieverts' constants are sometimes presented in literature in different units (e.g., the concentration represented in atomic fraction, i.e., $[\mathcal{S}_{X_2}^M] = 1/\sqrt{\mathrm{Pa}}$). In some of these cases the values had to be transformed using the temperature-dependent mass density for Pb-Li [17], which was done *before* applying the regression.

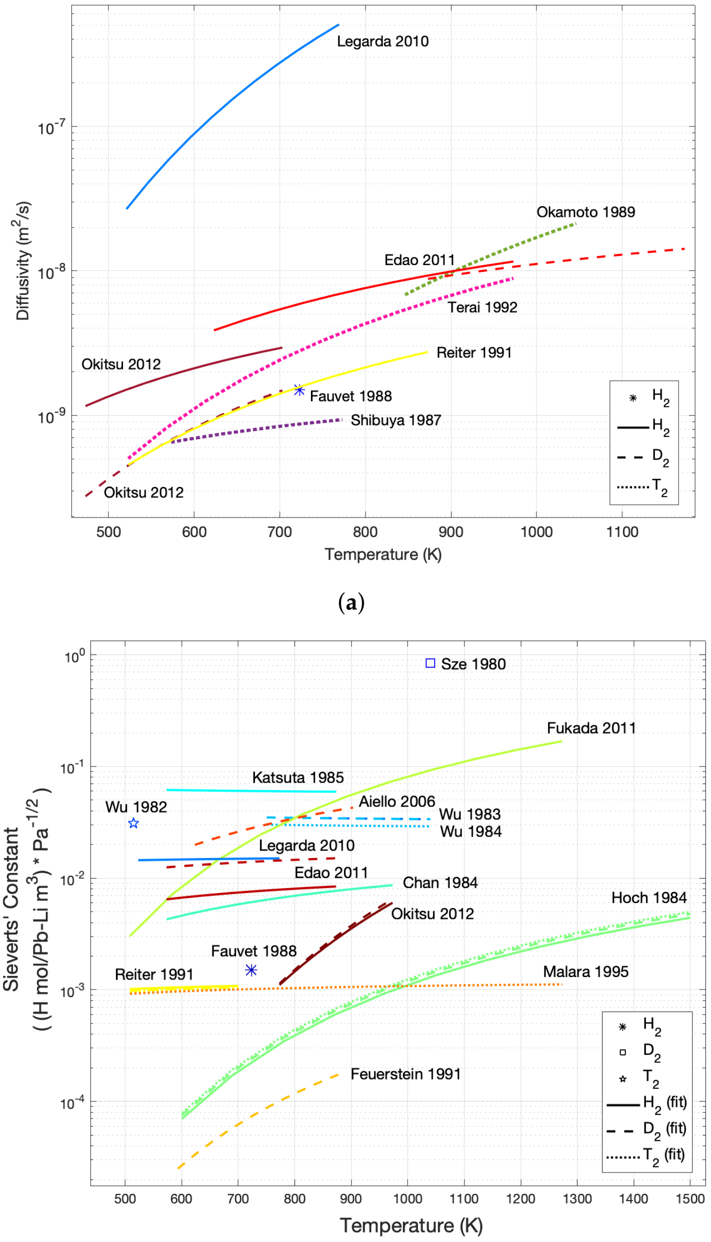

(**a**)

(**b**)

Figure 2. Literature review of $\mathcal{D}_{\mathrm{Q}}^{\text{Pb-Li}}$ and $\mathcal{S}_{\mathrm{Q}_2}^{\text{Pb-Li}}$. If only point values were available in any given reference, dissolution parameters were obtained by logarithmic regression after applying unit transformation. (**a**) Literature values and functions of diffusivity for hydrogen isotopes in Pb-Li [10,18–24]. (**b**) Literature values and functions of Sieverts' constant for hydrogen isotopes dissolution in Pb-Li [11,18,20,22–35]. When necessary, the temperature-dependent density of Pb-Li was used for unit conversion [17].

Some references reviewed in Figure 2a,b present not only experimental measurements, but also values obtained from theoretical models (e.g., thermodynamic model for alloys [26,32,33]). Some of those apply an extrapolation to obtain coefficients for one isotope based on the coefficient for another. This can be done using Equation (6) due to inertia's impact on the diffusivity.

$$\mathcal{D}_X^M \propto \left(\frac{m_M + m_X}{m_M \cdot m_X}\right)^{1/2} \implies \frac{\mathcal{D}_{X'}^M}{\mathcal{D}_X^M} \approx \sqrt{\frac{m_X}{m_{X'}}} \tag{6}$$

In it, m_X, $m_{X'}$ and m_M are the atomic masses of two gas isotopes and the metal, respectively [23]. Some references also apply this rationale to Sieverts' constant (e.g., [22]), however it is still debatable whether an isotopic dependence for $\mathcal{S}^M_{X_2}$ should be based on zero-point energy analysis instead [26,33,36–38].

A similar literature review of the diffusivity and Sieverts' constant for hydrogen isotopes dissolution in steel was also performed, as it was relevant for the work hereinafter. Graphs analogous to those presented here are shown in Section 4, alongside results of that section.

3. A Methodology to Differentiate Dissolution from Gas Losses in Gas-Metal Systems

3.1. Modelling Approach and General Assumptions

Figure 3 shows the proposed model to simulate experiments of gas dissolution in metals. The top of the image shows how a metallic barrier can be represented by a 1D diffusion channel. Any given metallic barrier can be represented by a single channel, that computes the average diffusion process through its total surface. The channel is sub-divided into nodes, which provide a mesh to apply a numerical method. In this work, the resulting system of equations was obtained with the inite Differences method, as usually presented in related literature (e.g., [39]). A Backwards Euler (implicit in time) 2nd-order (in space) scheme was applied to ensure model stability and limited truncation error without much computational cost [40,41].

The bottom of Figure 3 shows shows a diagram of the expected behavior of the concentration profile of a gas, and its evolution in time, inside a double metallic barrier. In this particular example, the diagram represents metals with similar Sieverts' constants, but significantly different diffusivities. Any discontinuous variation of medium properties requires the diffusion channel to be split into two sub-channels, solved in succession.

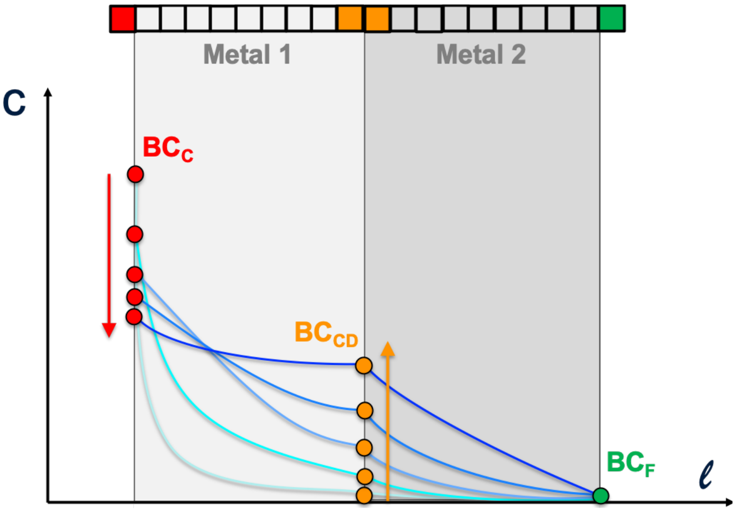

Figure 3. Representation of a generic double metallic barrier being simulated with the proposed model. The nodal division of the barrier provides a mesh along the channel length to apply a numerical method (**top**). In this example, the **left** side of the barrier experiences a finite amount of gas and the **right** side is ideally ventilated. The spatial concentration profiles in each metal evolve in time (**bottom**, in *blue*, from light to dark). Furthermore, in this example Sieverts' constants for both metals are assumed equal, so no profile discontinuity is seen at the interface. Three possible types of boundary conditions (BCs): Coupled BCs (in *red*), Co-Dependent BCs (in *orange*) and Fixed BCs (in *green*). When BC can also evolve in time, this is indicated by an arrow.

Below follows a list of additional general assumptions applied in the proposed model:

I Diffusion is not hindered by surface oxidation, chemical bonds or micro-structural defects (in case of solid medium) [14,33].

II Low pressure regimes imply that Sieverts' Law may be applied. Subsequently, in these conditions the gas concentration in a metal is low enough to allow one to approximate chemical-activity to concentration, with the purpose of computing the diffusion process in a single medium [7].

III Concentration gradients only exist in the direction of the diffusion channels, and temperature gradients along them are negligible. This way the diffusivity and Sieverts' constant do not vary along the diffusion channel. This can be assumed if the width of the metal barriers, along the dimension of the diffusion process, is considerably smaller than its other dimensions [14].

3.2. Boundary Conditions (BC) on a Double Metallic Barrier for the Dissolution of a Diatomic Gas

The boundary conditions (BCs) on the surface of a metal for a dissolution process simulated using this approach depend on the type of system being simulated. Bulk-controlled systems lead to Dirichlet BCs, i.e., the concentration value—in this work it is assumed that the gas phase density and the gas concentration in the solid can be used interchangeably—at the gas-metal interface is directly applied as BC, since dissociation and recombination at the surface are not limiting the diffusion process. On the other hand, surface-controlled systems lead to Neumann BCs, i.e., the derivative of the concentration at the gas-metal interface must be applied as BC, since surface fluxes limit the diffusion process. To apply this model to steel and Pb-Li, it is assumed that these metals are bulk-controlled (*vide* Section 2) and thus require only Dirichlet BCs; the methodology can nevertheless be extended to surface-controlled systems if surface dynamics coefficients are known (e.g., [13]).

As displayed in Figure 3, three possible types of BC are foreseen in the proposed model:

- **Coupled BC**: gas-metal interfaces exposed to a finite amount of gas experience a BC that changes in time, since the flow of particles through the metal surface alters the gas density outside the metal. If more than one diffusion channel is simulated, all BCs must be altered in unison, taking into account the amount of gas flowing through the boundary node of each channel. For this reason, these BCs are effectively coupled.
- **Co-Dependent BC**: metal-metal interfaces only present a change in medium properties and no other process is assumed (e.g., recombination/dissociation); that is, fluxes are not determined by surface-controlled aspects.
- **Fixed BC**: gas-metal interfaces exposed to a gas reservoir of infinite supply experience a BC constant in time. In the particular case that the BC is equal to zero (as shown in the example in Figure 3), the model represents a surface that acts as a perfect sink (i.e., that metallic surface is constantly and efficiently ventilated).

Figure 4 illustrates, through the simplified example of a single-metal barrier under equal conditions on both sides, how Fixed BCs are determined. The ideal gas law is used to compute a molecular density c_{X_2} outside of the metal using the gas pressure (i). Due to surface dissociation, the interface experiences an atomic density c_X (ii). Since Sieverts' Law establishes the atomic concentration of gas present inside the metal when in equilibrium (given that gas phase pressure p_{X_2}), Sieverts' concentration c_X^* is taken as a critical limit (maximum) to this concentration (iii). This agrees with the expected behavior of the diffusion process, that tends to a constant profile equal to c_X^* when in steady-state. Thus, the BC is taken as the minimum between c_X^* and the gas atomic density at the interface c_X.

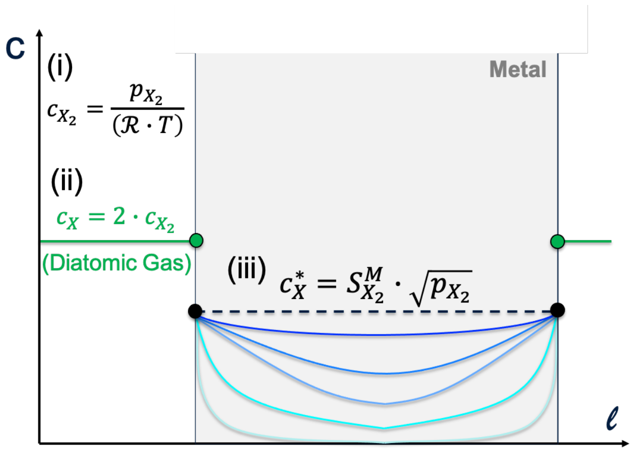

Figure 4. Diagram of BC determination at the gas-metal interface for a bulk-controlled single metallic barrier, when experiencing on both sides an infinite supply of diatomic gas at given temperature T and pressure p_{X_2}. (**i**) Calculation of gas density (c_{X_2}) at the metal surface with the ideal gas law. (**ii**) Calculation of the surface atomic concentration (c_X, in *green*) by multiplying the gas density by the number of atoms that compose the gas molecules, due to dissociation. (**iii**) The effective fixed BC applied is the minimum between the atomic concentration and Sieverts' concentration (c_X^*) for that gas pressure, obtained using Sieverts' constant ($\mathcal{S}_{X_2}^M$). This BC leads to concentration profiles evolving in time (in *blue*, from light to dark). The particular case of $c_X > c_X^*$ is represented; in equilibrium, the concentration inside the bulk tends to c_X^* (in *black*, dashed).

The procedure used for determining Fixed BCs can be applied to cases in which the gas pressure p_{X_2} varies in time. In these cases, since both c_X and c_X^* change in time, tasks (i)–(iii) are performed at every time step. In the particular case in which the fluxes through the gas-metal interface alter the pressure and multiple channels are simulated, the model presents Coupled BCs. One example of such scenarios is the simulation of a closed metal container during a static absorption experiment. A simulation with the model presented in this work can be used to compute the variation of the inner pressure in the container, caused by gas loss. Each container wall can be modelled by one diffusion channel, and the total gas loss in the container at each time step can be computed by multiplying the average atomic fluxes through each wall by that wall's area. The pressure decrease inside the container can be inferred with the ideal gas law, and the new pressure is subsequently used to define the Coupled BCs of the next time step.

Finally, for scenarios exhibiting double metallic barriers, Co-Dependent BCs must be computed. To do so, two continuity laws must be enforced: for the flux and for the chemical potential. In cases where the Sieverts' constant is similar for both metals, the chemical potential can be approximated to the concentration, which results in profiles as seen in Figure 3. In it, equating the fluxes exiting Metal 1 and entering Metal 2 leads to a discontinuity on the first derivative of the concentration profiles (blue lines), caused by the difference in diffusivities between metals. However, in cases where the Sieverts' constant varies significantly across the interface, the profiles themselves also present a discontinuity due to the different equilibrium distribution coefficients of each metal [42]. In these cases Equation (7) is used (alongside the flux continuity) to derive the concentration values *at the interface*, which act as the Co-Dependent BCs for each diffusion sub-channel.

$$\frac{c_X^{M_1}}{c_X^{M_2}} = \frac{\mathcal{S}_{X_2}^{M_1}}{\mathcal{S}_{X_2}^{M_2}} \tag{7}$$

The derived concentration values (i.e., Dirichlet BCs) can be re-calculated at each time step using the fluxes obtained at the previous one. This implies a non-implicit algorithm scheme; simulation stability and negligible error can then be ensured by increasing the number of space/time nodes.

3.3. Measurement of Diffusivity and Sieverts' Constant from Experimental Gas Pressure Evolution

The application of this model allows one to simulate the evolution of pressure inside a closed metal container, at a given temperature, if the dissolution parameters D_∞, S_∞, E_d and E_s are known. However, dissolution parameters are not always known (e.g., literature scattering for Pb-Li, lack of steel manufacturer's data); in these cases, comparison of the simulated pressure decrease curve with an experimental one allows for the determination of the dissolution parameters through a "curve matching" strategy.

To apply this curve-matching strategy, the simulation must be run several times. Each time a pressure decrease curve is simulated with a particular combination of dissolution parameters (D_∞, S_∞, E_d and E_s). These combinations are made by varying each parameter inside its respective range between extreme values (maximum and minimum), derived from literature using logarithmic regression (*vide* Section 2). The resulting simulated curves can be compared to the experimental pressure curve; the one that displays smallest least-squares deviation is assumed to have been simulated using dissolution parameters closest to the real values.

The determination of dissolution parameters through the curve-matching strategy applied to an experiment of gas loss from a metal chamber effectively provides one with the diffusivity and Sieverts' constant for that gas-metal pair as a function of temperature. Notice how modelling double metallic barriers allows one to apply the model to experiments containing two metals (e.g., steel and Pb-Li).

Subsequent comparison of the diffusivity and Sieverts' constant to literature measurements allows for the validation of the proposed model and methodology. Section 4 presents how an experiment with deuterium in a steel container was modelled using this approach, and the resulting dissolution parameters for the 316L steel that made up that container.

4. Methodology Validation by Comparing Simulations and Experiments of a Deuterium-Steel System (without Pb-Li)

4.1. Simulating a Deuterium Pressure Decrease Curve in the VST Upper Chamber

Figure 5 shows the length measurements of a setup of interest to be modelled: the Upper Chamber (UC) of the Vacuum Sieve Tray (VST) experiment [8]. As a *geometrical-system simplification* to apply a numerical model, fittings were neglected and the chamber was considered an assembly of only three parts: the LID, the WALL and the BASE. Both the LID and the BASE can be considered solid cylinders, and the WALL a hollow cylinder, all made of uniform 316L steel, which supports Assumption I [14].

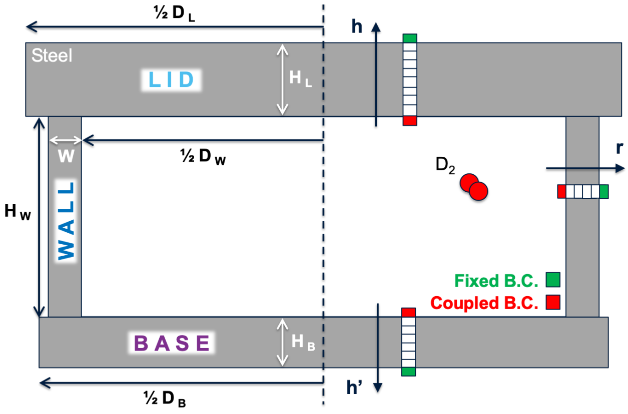

Figure 5. Schematic of the VST Upper Chamber (UC) as modelled using a quasi-2D modelling approach. The dashed line indicates an axis of cylindrical symmetry. On the left, simplified chamber dimensions used in the model ($D_L = 305.0$, $D_W = 250.0$, $D_B = 270.0$, $H_L = 26.0$, $H_W = 95.0$, $H_B = 20.0$, $W = 2.0$; all in mm). On the right, a diagram of the diffusion channels foreseen in the simulation (two cartesian vertical, h and h', and a cylindrical radial, r). Boundary conditions are indicated by color: external Fixed BC (in *green*) and internal Coupled BC (in *red*).

Experiments of interest with the UC foresaw injecting a fixed amount of deuterium gas (D_2) inside the chamber and then observing the pressure decrease along time. The technical limitations of the setup forbade an initial pressure in the UC higher than 1.5 bar, so $\approx 5 \times 10^{-2}$ mol were chosen as injection amount. This amount ensured initial pressures of ≈800 mbar in the experiments with the highest foreseen temperatures. This complied with the former requirement and also ensured reliable accuracy for pressure measurements. Notice that this order of magnitude for the deuterium pressure is considerably smaller than its critical pressure (≈16 bar) [43], which supports the usage of the ideal gas law and Assumption II.

Figure 5 also shows how the model introduced in Section 3 was applied to the UC. Due to the present symmetries, a quasi-2D approach was deemed sufficient: each chamber part was modelled with a single (1D) diffusion channel along a different dimension. The channel lengths (H_L, H_B and W) are considerably smaller than all other measurements, which supports Assumption III [14].

Modelling surfaces exposed to the same finite amount of gas implied that the inner surfaces of the chamber had to be considered coupled (*vide* Section 3). Thus, all nodes representing the interior of the chamber were modelled as Coupled BC (in *red*, Figure 5). The exterior of the chamber was assumed to be a perfect sink for the diffusion process. Thus, nodes representing the exterior were modelled as Fixed BC (in *green*, Figure 5) with null concentration.

Due to their temperature dependency, the diffusivity and Sieverts' constant for deuterium dissolution in 316L steel had to be computed as a function of time for each experimental scenario simulated. For this, additional simulation inputs were planned in the form of the evolution of single surface temperature measurements for each chamber part (LID, WALL and BASE). The UC is fully covered by thermal insulation and the temperature of the chamber parts are determined by a controlled ohmic heater underneath the BASE [8]. Upon choosing a set-point, the gas was planned to be injected only after general thermal steady-state conditions were registered for any chamber part (temperature variations below 1% between subsequent measurements).

At each time step of the simulation, the BASE and LID temperatures (T_B and T_L, respectively) could be used to compute the diffusivity and Sieverts' constant on those chamber parts, interpolating values in time between measurements when necessary. In contrast, the WALL surface measurement could not be deemed representative of the whole chamber part; instead, the WALL temperature (T_W) was assumed to display a spacial linear profile, analogous to a metal rod connecting two thermal baths, with extremes T_B and T_L. This relies on assuming, as a *thermal-system simplification*, homogeneous distributions for the LID and BASE temperatures in comparison to the WALL, which is strongly suggested by the difference in metal volumes: the LID and the BASE have volumes approximately one order of magnitude higher than the WALL ($19.0 \times 10^5\,\mathrm{mm}^3$ and $11.4 \times 10^5\,\mathrm{mm}^3$, respectively, versus $15.0 \times 10^4\,\mathrm{mm}^3$). This approach was supported by the measurements on the single WALL surface sensor (placed approximately 20 mm from the heater). The deviation between the measurements and the theoretical value obtained with the linear temperature profile (temperature gradient of approximately 1 K/mm along the WALL) was considered negligible (≈0.06%) for the maximum heater set point of 450 °C.

Given the temperature variation on the WALL, computing the average diffusion process through this chamber part (with a single diffusion channel) required determining average values for the diffusivity ($\overline{\mathcal{D}_{\mathrm{D}}^{\mathrm{WALL}}}$) and Sieverts' constant ($\overline{\mathcal{S}_{\mathrm{D}_2}^{\mathrm{WALL}}}$). Due to their Arrhenius dependency (*vide* Equations (4) and (5)), and the linear temperature profile of the medium, Equation (8) was used to compute $\overline{\mathcal{D}_{\mathrm{D}}^{\mathrm{WALL}}}$ and $\overline{\mathcal{S}_{\mathrm{D}_2}^{\mathrm{WALL}}}$ (here shown as $\overline{K}$).

$$\overline{K} = \frac{1}{T_B - T_L} \int_{T_L}^{T_B} \kappa_1 \, e^{-\frac{\kappa_2}{\mathcal{R} \cdot T}} \, dT \qquad (8)$$

In it, κ_1 is the desired infinite-temperature coefficient (D_∞ or S_∞) and κ_2 its respective activation energy (E_d or E_s). Since T_B and T_L can be assumed homogeneous, this procedure is not required for the BASE nor the LID.

Given the lack of manufacturer data for the parameters κ_1 and κ_2 for the 316L steel used in the UC, planning of the experiments was performed with initial simulations run using literature-averaged dissolution parameters, as indicated in Table 1. While activation energies were arithmetically averaged, infinite-temperature coefficients were geometrically averaged due to their logarithmic scattering. To perform the averages, deuterium diffusivities were extrapolated (using Equation (6)) when data could be found only for other isotopes. Sieverts' constants were assumed to be the same for every isotope (i.e., neglecting zero-point energy differences), as mentioned in literature to be a good approximation for steel [12]. For comparison, the table also shows the literature extremes of the dissolution parameters.

Table 1. Average and extreme values of dissolution parameters for deuterium dissolution in 316L steel, derived from literature and applied in the simulations [12,14,44,45].

316L (D_2)	D_∞ ($\mathrm{m^2/s}$)	E_d ($\mathrm{kJ/K{\cdot}mol}$)	S_∞ ($\mathrm{mol/m^3 \cdot 1/\sqrt{Pa}}$)	E_s ($\mathrm{kJ/K{\cdot}mol}$)
max	9.20×10^{-7} [44]	66.10 [45]	1.50×10^{0} [12]	20.58 [12]
avg	1.41×10^{-7} (all)	52.24 (all)	6.57×10^{-1} (all)	13.46 (all)
min	5.77×10^{-9} [45]	42.50 [12]	2.82×10^{-1} [14]	6.70 [45]

Initial simulations were run using a set of temperature measurements obtained during a trial run of the experiment with no gas. Convergence tests were performed both for spacial node and time node counts. Test were done for powers of 10, between 10^1 and 10^5. No significant precision is gained by simulating meshes with more than 10^3 nodes (relative difference between figure of merits of subsequent simulations below 0.05%), so subsequent simulations utilized this mesh resolution.

Results of these initial simulations can be seen in Figure 6, which shows the evolution of the atomic concentration of deuterium both in the BASE and the WALL. Notice how the profile in the WALL (Figure 6a) evolves faster than in the BASE (Figure 6b), even though it displays a linear temperature profile with a lower average (≈405 °C). This is attributed to the steeper concentration gradients in the thinner medium, which is the dominating diffusion drive in comparison to the temperature effect on the diffusivity and Sieverts' constant.

As expected, concentration curves evolve towards linear profiles connecting the BCs (*dashed* lines). However, it should be noted that these linear profiles correspond to a *pseudo*-steady-state (PSS). As the simulation takes into account the pressure decrease inside the chamber, the Coupled BCs (left, in *red*) are recalculated at every time step and tend to decrease with time (*vide* Figure 3). The displayed *dashed* lines only describe the last simulated time step—in other words: a pseudo-steady-state profile indicates the future tendency of the concentration profile curves only if the BCs became Fixed BCs at that time.

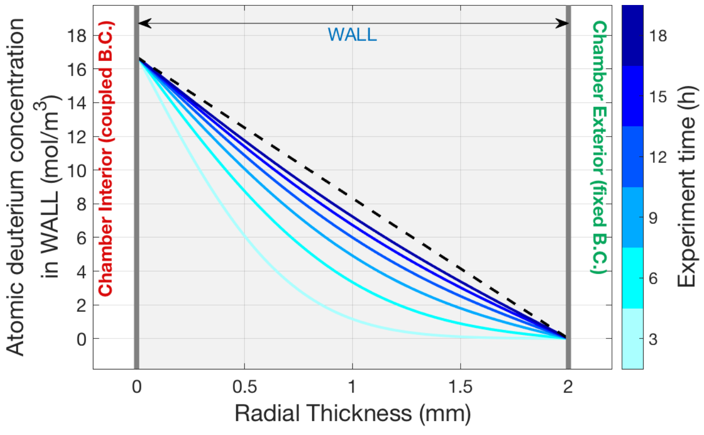

(**a**)

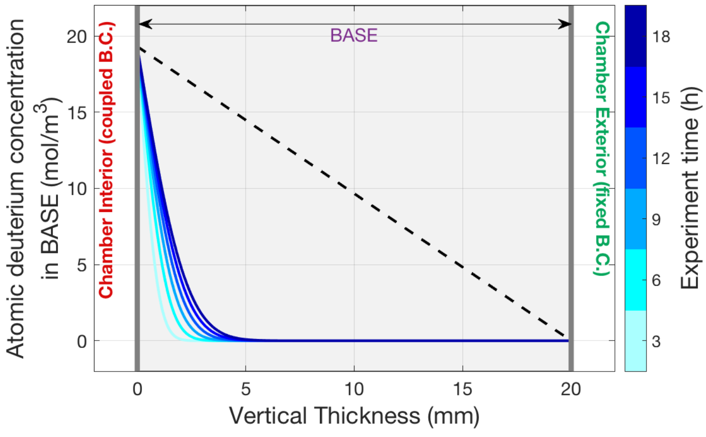

(**b**)

Figure 6. Simulation of concentration profiles evolution during 18 hours in the WALL and BASE steel media, using **avg** dissolution parameters (*vide* Table 1). Initial gas pressure set to 780 mbar and BASE temperature set to 450 °C, to be representative of experiments performed with the heater set at that temperature. The difference in medium thickness (of one order of magnitude) leads to steeper concentration gradients that ensure the profile evolves faster in the WALL than in the BASE, in spite of the WALL having a lower average temperature (≈405 °C). Profiles tend towards pseudo-steady-state (PSS; *dashed* lines), which represent the expected steady-state profiles computed using the BCs of the last time step. (**a**) Concentration profile evolution in the WALL. Medium thickness of 2 mm. (**b**) Concentration profile evolution in the BASE. Medium thickness of 20 mm.

4.2. Experiments with the VST Upper Chamber

Three experimental runs were performed with the UC of the VST setup. Before each experiment, a bake-out procedure was performed to ensure the removal of any gas trapped in the chamber metals. The initial bake-out was done for 96 h; subsequent bake-outs were done for a minimum of 16 h. During bake-out, the ohmic heater temperature was always set at maximum (450 °C) while the interior of the chamber was continuously evacuated. After each bake-out, pumping was maintained and the ohmic heater was set to a given desired temperature. Bake-out plus thermal development periods (until general steady-state, *vide* Section 4.1) lasted for a minimum of 24 h—these periods were purposefully increased if gas trapping from the previous experiment was deemed more significant, either because of a longer experiment or higher temperatures.

Experiments were performed with the following heater set temperatures: 100 °C, 350 °C and 400 °C; the latter two being the most relevant for fusion energy applications. In each case, deuterium was injected for 34 ± 2 s at the maximum flow rate of 2600 ± 26 SCCM ("standard cubic centimeter per minute", approximately equivalent to 7.4×10^{-7} mol/s). The maximum rate was chosen to reduce injection time and increase representativity of the computational model, which assumes the process starts from an instantaneous onset of pressure. The measured pressure decrease was corrected using a calibration dependent on the temperature of the pressure sensor.

4.3. Applying Curve-Match to Obtain Dissolution Coefficients for the VST's 316L Steel

As introduced in Section 3, the dissolution parameters D_∞, S_∞, E_d and E_s for a gas-metal pair can be determined using the curve-matching strategy proposed. For that, each parameter was varied between the literature extremes (*vide* Table 1), subdividing these ranges in 10 steps per parameter (for a total of 10^4 pressure decrease simulations per experiment).

Figure 7 shows the measured pressure decrease curves for the experiments and their respective simulated curves for simulations run with the dissolution parameters determined through curve-matching. All curves display two phases:

- the first one shows a faster pressure decrease and lasts for only a fraction of the total experiment time (roughly: 15 h for the experiment at 100 °C, and less than 1 h for the others);
- the second one shows an apparent linear (and slower) pressure decrease (after the first phase ends).

The correlation between experimental temperatures and time for the transition between first and second phases is explained by the increase of diffusivity with temperature.

The first phase corresponds to larger fluxes of deuterium gas diffusing through the metal parts, caused by steeper concentration gradients (as exemplified by the *light blue* lines on Figure 6), which lead to a sharp pressure decrease in the beginning. The second phase corresponds to smaller fluxes, because the system is close to pseudo-steady-state conditions (*dark blue* lines tending to *dashed black* lines on Figure 6). These phases could be considered similar to the diffusive and permeative stages of the theoretical dissolution process, as defined in Section 2. However, it should be noted that these stages are not technically equivalent to the first and second curve phases, respectively, because this type of experiment is not expected to ever reach true steady-state conditions (i.e., permeative stage). Since the amount of gas in the chamber is finite, the metal experiences a pressure decreasing in time, and thus, BCs that change in time. This is successfully taken into account by the model presented in this work with the implemented Coupled BCs on the inner side of the chamber, that are recalculated at every time step.

In fact, it should be noted that Richardson's Permeation Law, often applied in literature to compute passage of gases through metals [12,14], is not capable of computing the first phase of the curves presented, since it would assume pseudo-steady-state conditions from the start of the experiment. Since the pressure decrease in the first phase amounts to a significant portion of the total pressure decrease (especially for experiments made at lower temperatures and for shorter periods of time, e.g., Figure 7a), such approach should not be used in static absorption/desorption experiments. Contrary to that, the model presented in this work is able to properly simulate the pressure decrease in a metallic chamber both *before and after* pseudo-steady-state conditions have been reached.

Experimental and simulated pressure decrease curves present the same qualitative behavior in Figure 7a–c. In particular, good agreement can be seen in Figure 7a, where pressure fluctuations attributed to temperature variation in the laboratory environment during the period of a day were also reproduced by the model. The only modest discrepancy, visible in Figure 7c, is the sharper pressure decrease in the first phase of the simulated curve, in comparison to the experimental one. This is explained by the injection process in the experiments (not shown in Figure 7 due to scale), which is considered instantaneous in the simulations. Due to the real finite injection rate, the process lasts for a non-null period of time ($\Delta t_{\text{inject}} \neq 0$). During this time, the quantity of gas in the chamber increases due to the injection, but also decreases due to diffusion already taking place through the metallic walls. As it can be seen in Figure 8, the net effect is an underestimated initial pressure used as input for the simulations (p_{init}), which would lead to simulated pressure decrease curves lower than experimental ones. However, as the curve-match procedure aims at determining the set of dissolution parameters that minimizes the overall least-squares deviation between experimental and simulated curves, it tends to raise the simulated pressure curve by decreasing D_∞ and S_∞, and increasing E_d and E_s, to compensate. This effect was taken into account and mitigated by performing longer experiments, to reduce the overall weight of the first phase of the pressure decrease curves in the deviation calculation, and thus on the dissolution parameters estimates. In other words, this discrepancy did not meaningfully affect the results.

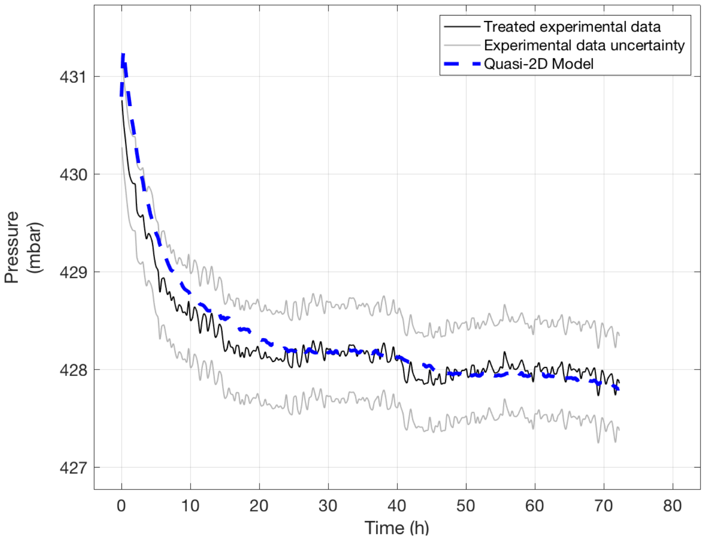

(**a**)

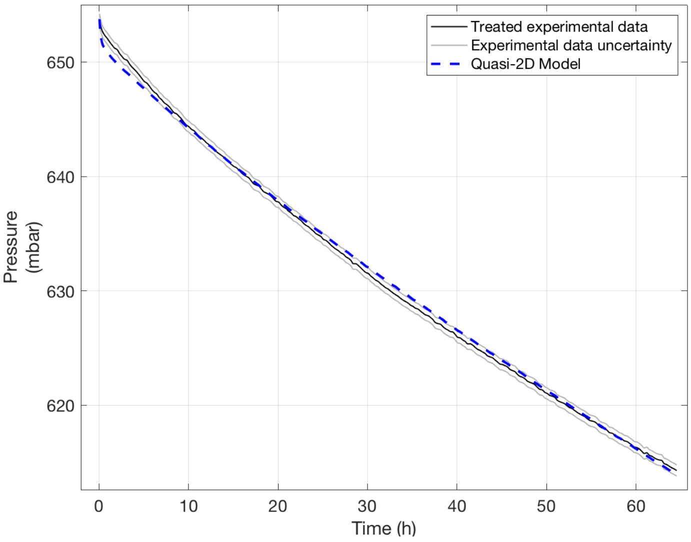

(**b**)

Figure 7. *Cont.*

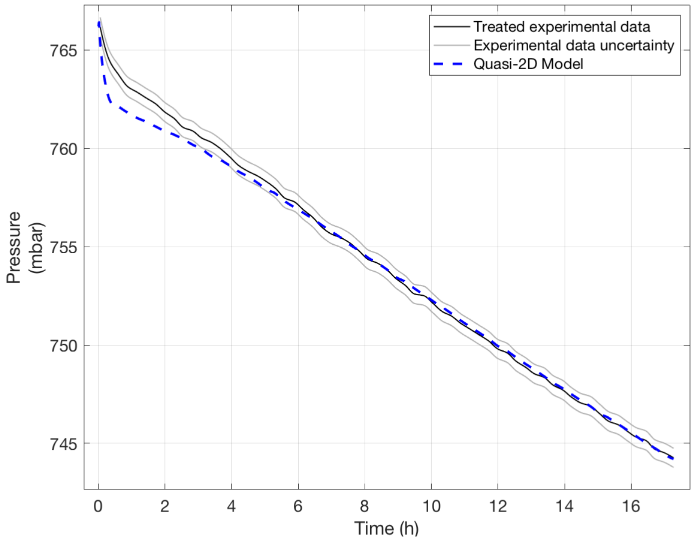

(**c**)

Figure 7. Comparison between the experimental and simulated curves for the pressure decrease in the VST UC during the deuterium experiments, for three different temperatures. Propagated uncertainty for experimental data is displayed with two extra curves (in *gray*) to increase visibility. Simulated curves use dissolution parameters determined by the curve-matching strategy (*vide* Table 2). Increased data fluctuation seen in (**a**) results from: the graph scale (due to a smaller total pressure variation during the experiment), and a larger set of collected experimental points. (**a**) Experiment and simulation for heater set at 100 °C. (**b**) Experiment and simulation for heater set at 350 °C. (**c**) Experiment and simulation for heater set at 400 °C.

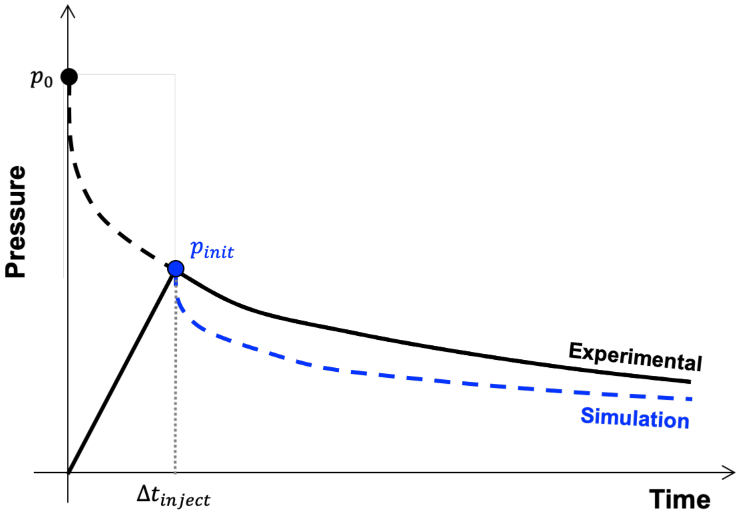

Figure 8. Visualization of the difference between first pressure points in simulated curve (p_{init}) and experimental curve (p_0), and the resulting effect that simulated pressure decrease curves are necessarily lower than experimental ones. The value p_0 is equivalent to the pressure associated with all the gas injected in the UC if no dissolution happened, and cannot be directly measured. The value p_{init} is chosen as the first pressure measurement after injection, that does not coincide with p_0 due to the finite injection rate. An infinite injection rate would lead to $\Delta t_{\text{inject}} = 0$ and allow one to measure p_0.

Table 2 displays the estimated parameters and Figure 9 shows the diffusivities and Sieverts constants calculated with them in function of temperature. The figure also displays curves derived from literature, in a similar fashion as the ones presented for Pb-Li (*vide* Section 2). As it can be seen, the results of this work are in good agreement with literature, which shows that the methodology developed here is considered suitable for the determination of dissolution parameters (and thus, diffusivity and Sieverts constant) of deuterium dissolution in 316L steel.

As seen in Figure 9a, the diffusivity obtained in this work is somewhat higher in comparison to other values reported in literature. This was attributed to an ultimate underestimation by the simulation of the total gas loss experienced by the metal chamber; and a subsequent attempt of the curve-match procedure to adjust for that by assuming a larger diffusivity for deuterium in steel. A study was performed to assess whether the geometric simplification of the UC was responsible. Assuming that the steel thickness of the fittings are the same as the chamber parts to which they are attached, the total inner surface of each part and the total inner volume of the chamber were altered to include the dimensions of the fittings in the simulations. However, the net effect of this adjustment was a change in the total pressure loss of only ≈0.5%, which corresponds to ≈0.03% in terms of absolute pressure variation. This is explained by the competing effects that inner surfaces and chamber volume have on the model:

- a larger volume decreases the pressure calculated at each time step, which reduces the Coupled BCs experienced by the inner surfaces, thus reducing the surface density of escaping molecular flows; but,
- larger inner surfaces increase the total escaping molecular flows.

This implies a limited impact of neglecting the fittings in the UC model: the additional pressure loss can be singly attributed to the fact that fittings have thinner steel thicknesses than the chamber parts, which leads to steeper concentration gradients and increased diffusion flows (*vide* Figure 6). That is to say, the dissolution parameters estimated by the curve-match procedure could moderately gain accuracy by adding (a) diffusion channel(s) to the UC model that represent(s) the fittings.

As also seen in Figure 9a, the estimated dissolution parameters for the diffusivity (D_∞ and E_d) lead to a consistent behavior across the temperature range of all experiments (100–400 °C). In Figure 9b, however, the estimated dissolution parameters for the Sieverts' constant (S_∞ and E_s) in the experiment performed at 100 °C present a slight disagreement with the ones performed at 350 °C and 400 °C. This can be explained by the smaller pressure decrease induced by lower temperatures: ≈3 mbar loss over 70 h of experiment at 100 °C, as opposed to ≈30 mbar loss in the experiment of similar duration at 350 °C. This limited pressure loss affects the accuracy of measurements, which impacts the precision of the curve-match procedure, as multiple sets of dissolution parameters can retrieve curves inside the uncertainty range. This implies a higher fidelity in the dissolution parameters for the Sieverts' constant (particularly S_∞) estimated from experiments at 350 °C and 400 °C.

Taking the comparison between experiments and simulations into account, it was concluded that the model is able to reproduce the dissolution of deuterium in steel during both curve phases, when using the dissolution parameters estimated by the curve-match procedure. Given the comparison of the diffusivity and Sieverts' constant obtained with these parameters to literature results, the methodology was considered *validated*.

Table 2. Dissolution parameter estimates from applying the curve-matching procedure to the experiments presented in this work.

316L (D_2)	D_∞ (m^2/s)	E_d (kJ/K·mol)	S_∞ ($mol/m^3 \cdot 1/\sqrt{Pa}$)	E_s (kJ/K·mol)
100 °C	7.17×10^{-7}	42.50	1.50×10^{0}	12.87
350 °C	8.18×10^{-7}	42.50	5.50×10^{-1}	17.50
400 °C	5.14×10^{-7}	42.50	4.20×10^{-1}	15.95

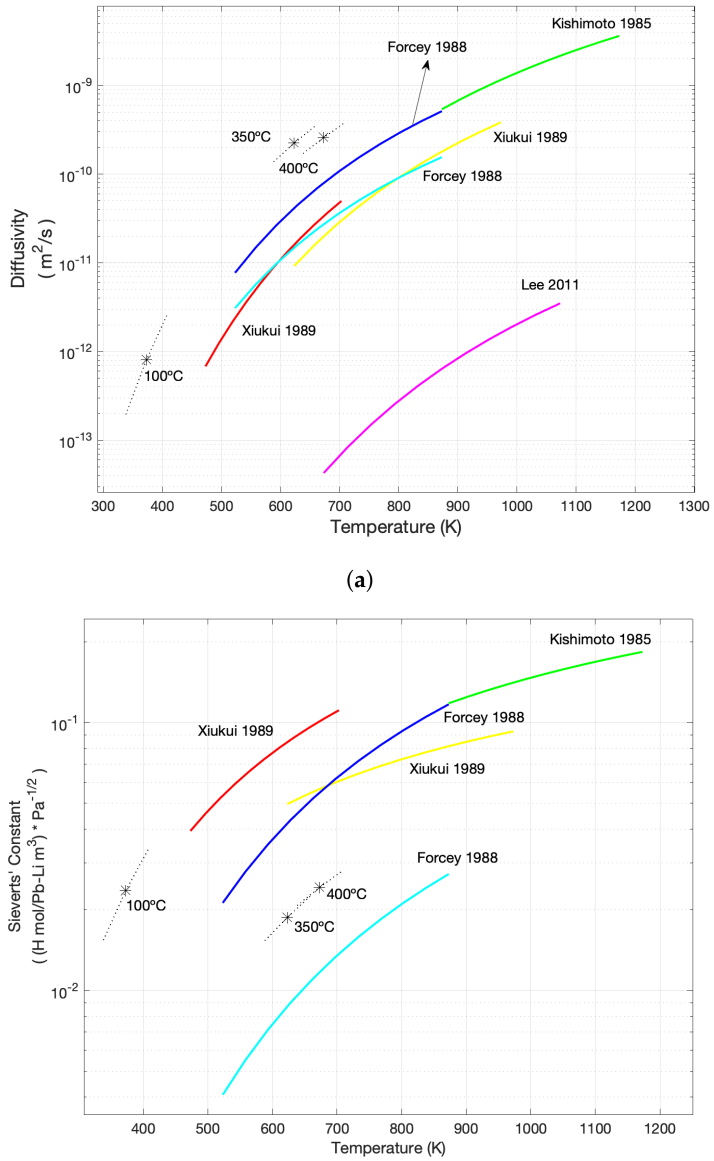

(**a**)

(**b**)

Figure 9. Comparison between literature functions of $\mathcal{D}_{\mathrm{D}}^{316\mathrm{L}}$ and $\mathcal{S}_{\mathrm{D}_2}^{316\mathrm{L}}$ (coloured), and those determined by the curve-matching strategy (in *black*, *vide* Table 2). As each experiment provided a set of dissolution parameters, the general behaviour of the Arrhenius Law around the temperature set for the experiment (*asterisk* markers) is displayed by curve extensions (*dotted* lines). (**a**) Comparison between literature functions of diffusivity for deuterium in 316L steel [12,14,44,45], and from set of dissolution parameters (D_∞ and E_d) derived in this work. (**b**) Comparison between literature functions of Sieverts' constant for deuterium in 316L steel [12,14,44], and from set of dissolution parameters (S_∞ and E_s) derived in this work.

5. Simulation of Future VST Experiments with Pb-Li Using Literature-Averaged Dissolution Parameters

The validated model presented in this work was then used to simulate an experiment similar to the one presented in Section 4, but this time including liquid Pb-Li in the UC. As an initial study to help plan for future experiments with the VST setup using Pb-Li, literature-averaged parameters for deuterium dissolution in both 316L steel (*vide* Table 1) and Pb-Li (*vide* below) were applied to these simulations, to evaluate the following averages: time required to reach dissolution equilibrium and expected pressure decrease in the chamber.

5.1. Simulating the VST Upper Chamber + Pb-Li System with Literature-Averaged Dissolution Parameters for Pb-Li

Because of the large current scattering in measurements of dissolution parameters for hydrogen isotopes in Pb-Li, simulations were run using literature-averaged values. Table 3 shows the literature extremes and averages of dissolution parameters for deuterium in Pb-Li, derived using the logarithmic regression method (*vide* Section 2 and Figure 2). Averages were obtained the same way as previously described. Some infinite-temperature diffusivity coefficients for deuterium were extrapolated from literature reports of hydrogen isotopes experiments, using Equation (6). In these cases, the activation energy was assumed to be the same for all isotopes. No extrapolation was performed for Sieverts' constants; only deuterium data directly found in literature was used.

Table 3. Average and extreme values of dissolution parameters for deuterium in Pb-Li [11,18,20,22–35].

Pb-Li (D_2)	D_∞ ($\mathrm{m^2/s}$)	E_d ($\mathrm{kJ/K{\cdot}mol}$)	S_∞ ($\mathrm{mol/m^3 \cdot 1/\sqrt{Pa}}$)	E_s ($\mathrm{kJ/K{\cdot}mol}$)
max	1.72×10^{-4} [18]	41.83 [19]	5.40×10^{0} [23]	54.44 [23]
avg	2.49×10^{-7} (all)	24.05 (all)	4.71×10^{-2} (all)	16.65 (all)
min	3.21×10^{-9} [10]	6.63 [10]	1.24×10^{-3} [22]	−0.93 [30]

When applying literature-averaged dissolution parameters:

- the calculated curve for the diffusivity of deuterium in Pb-Li is roughly *three* orders of magnitude higher than in steel;
- the calculated curve for the Sieverts' constant of deuterium in steel is roughly *one* order of magnitude higher than in Pb-Li.

This implies that the gas diffuses more quickly through Pb-Li (as expected, since it is a liquid medium, while steel is a solid), so its profiles evolve faster than in steel. On the other hand, since the Sieverts' concentration (*vide* Equation (3)) in Pb-Li is smaller than the one in steel, the BC experienced by steel surfaces that are covered by Pb-Li is smaller than the BC experienced by steel surfaces in contact with deuterium in gaseous form. This is true whenever the gas availability outside of the metals is not a limiting factor (i.e., $c_X < c_X^*$ case, as opposed to case shown in Figure 4). Notice that this difference will be maintained during the dynamic evolution of the system, until the Pb-Li layer is completely saturated with deuterium (at which point steel will experience the same BC as steel surfaces in direct contact with the gas).

Figure 10 shows the modelling approach applied to the UC, now containing Pb-Li. The interface between Pb-Li and the BASE in channel h' can be treated using a Co-Dependent BC, as introduced in Section 3.2. Because of the Sieverts' constant scattering, its calculation relied on Equation (7) to ensure the continuity of the chemical potential instead of the concentration. During the system transient, the aforementioned difference between BCs experienced by "wet" and "dry" steel surfaces implies that the flux through wet surfaces will be lower than through dry surfaces. Additionally, since future experiments with Pb-Li in the UC are designed with the height of liquid metal around 20.0 mm, the WALL surface that is wet is only ≈20% of the total. Thus, as a *mass-transport-system simplification*, radial diffusion was neglected through WALL sections covered by Pb-Li.

Figure 11 shows the evolution of atomic concentrations in the Pb-Li and the BASE for a simulation run at 450 °C and initial pressure of 780 mbar. Notice that the interface between Pb-Li and steel is represented in different positions in each graph; the interface concentrations are displayed at the abscissa $x = 18$ mm in Figure 11a, and abscissa $x = 0$ mm in Figure 11b. As previously explained, this interface concentration in Pb-Li is considerably lower than in steel; however, the deuterium flux is nevertheless directed from the former towards the latter because of the different chemical potential (represented by Sieverts' concentrations) of deuterium in each medium.

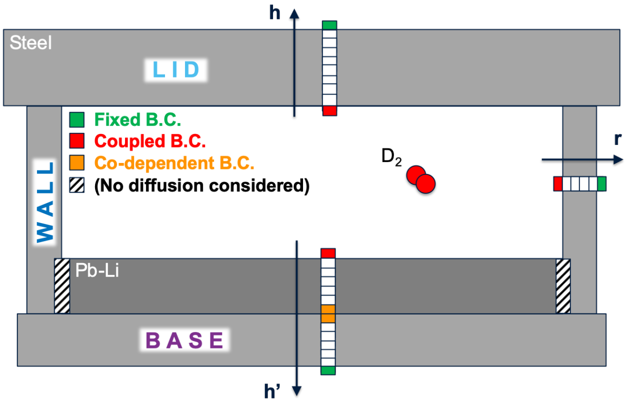

Figure 10. Schematic of the VST's Upper Chamber as modelled using the quasi-2D modelling approach for simulations that include Pb-Li. No radial diffusion is assumed for the WALL surface covered by Pb-Li. The lower vertical diffusion channel is extended to double metallic barrier channel, with a set of Co-Dependent BCs at the metal-metal interface (in *orange*).

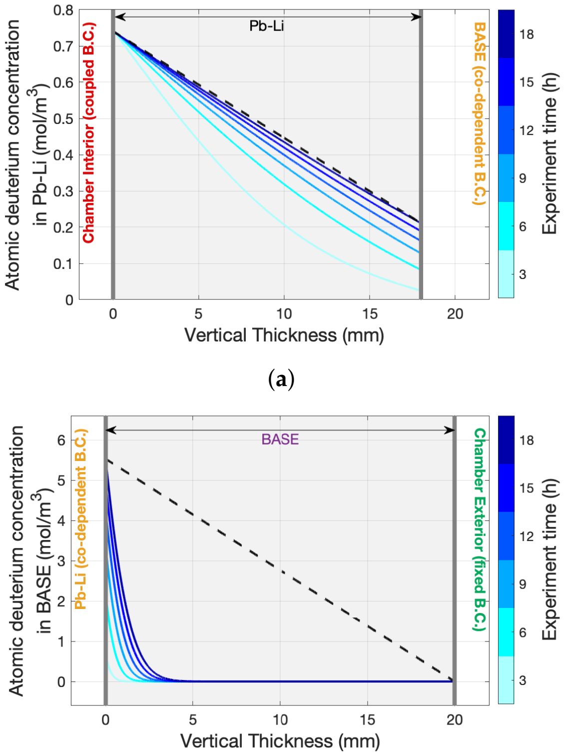

(**a**)

(**b**)

Figure 11. Simulation of concentration profiles evolution during 18 h in Pb-Li and BASE steel media, using **avg** dissolution parameters (*vide* Tables 1 and 3). Initial gas pressure set at 780 mbar, heater temperature set at 450 °C. (**a**) Concentration profile evolution in Pb-Li. Concentration maximum in the order of 8×10^{-1} mol/m^3. Medium thickness of 18 mm. (**b**) Concentration profile evolution in BASE. Concentration maximum in the order of 5 mol/m^3. Notice the difference in concentration scale in comparison to Figure 6b.

The concentration at the Pb-Li side of the interface rises with time. Due to the different diffusivities in each medium, deuterium arrives at the interface quicker than it transfers into steel, even if steel presents a higher affinity for the deuterium atoms. This leads to an accumulation in Pb-Li, which rises the interface concentration. This difference in diffusivities can also be seen by how much the 18 h profile in Pb-Li (Figure 11a) is closer to reaching its pseudo-steady-state than its counterpart in steel (Figure 11b).

Still focusing on the 18 h profiles, it should also be noted that the leftmost concentration in the BASE:

- is approximately 20 mol/m^3 in the simulation *without* Pb-Li (*vide* Figure 6b);
- but is only approximately 5 mol/m^3 in the simulation *with* Pb-Li (*vide* (Figure 11b);

under the same temperature and pressure conditions. This difference is again explained by the one order of magnitude difference between Sieverts' constants assumed for steel and Pb-Li. It leads to a temporarily bounded concentration in Pb-Li that limits the maximum BC that steel can experience. This implies that Pb-Li acts as a *permeation barrier* to steel. This also supports neglecting fluxes through the lower, wet sections of the WALL surfaces while Pb-Li is not saturated, as it was assumed for the developed model.

The consequences of different evolution speeds in each medium can also be visualized by spacial integration of the concentration profiles, which provides the total amount of gas dissolved in each medium. The evolution of these values simulated for 288 h (12-days experiment) can be seen in Figure 12a, given in molecular form—the gas is dissolved in atomic form, but values in molecular form allow for easier comparison with injection amounts to determine how much deuterium gas is lost from the chamber. Notice how in this period Pb-Li reaches a relatively stable amount of dissolved gas, while the curves for the LID and the BASE still present positive, non-negligible derivatives in time at the end of the simulation. The same cannot be said about the WALL, that reaches medium saturation much more quickly, ultimately attributed to its thinner dimension.

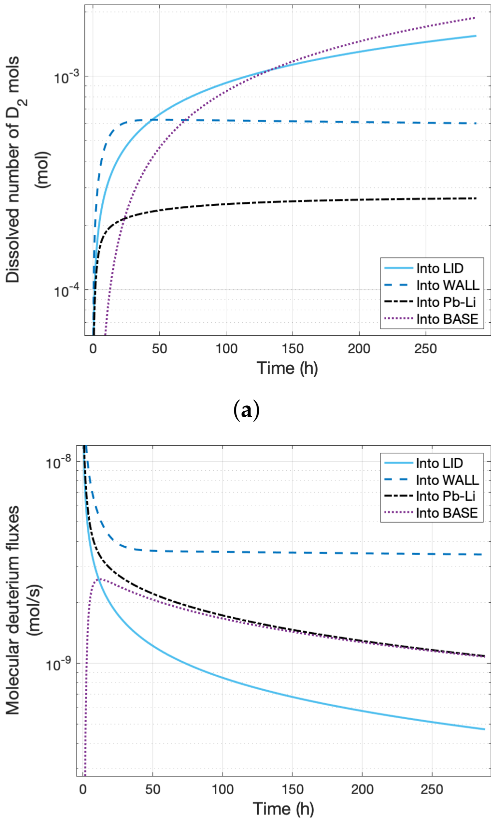

(**a**)

(**b**)

Figure 12. Evolution of number of moles dissolved in, and fluxes through, each UC part for a simulation of 288 h, using **avg** dissolution parameters (*vide* Tables 1 and 3). Values given in molecular amounts, instead of atomic, for easier comparison with the amount of gas injected in the chamber. Initial gas pressure set to 780 mbar and BASE temperature set to 450 °C. (**a**) Evolution of the equivalent molecular number of moles of deuterium dissolved, in logarithmic scale. (**b**) Evolution of the equivalent molecular fluxes of deuterium, in logarithmic scale. Fluxes into Pb-Li and into BASE tend to the same value as the system tends to an equilibrium state.

Figure 12a also shows that the amount of deuterium trapped in the BASE is significantly smaller than in the LID for the initial period of evolution. This is true in spite of their temperature difference, that favors diffusion into the former (temperatures were assumed similar to the ones in experiments without Pb-Li; e.g., LID at ≈362 °C when the BASE is at 450 °C). This is attributed to the permeation barrier effect brought by Pb-Li, that considerably reduces the fluxes entering the BASE in the beginning of the process.

Such fluxes can be derived using Fick's Law (*vide* Section 2). Figure 12b shows the fluxes entering each metal by their innermost surface in respect to the center of the UC. The curves displayed confirm that fluxes through the inner surface of the WALL reach equilibrium conditions much faster than for other UC parts. However, although one can verify that fluxes into the Pb-Li and BASE approach the same value (as expected) as the complete system tends to equilibrium, these curves do not display negligible derivatives in time after 288 h. This implies that the system is close to equilibrium but the Pb-Li is not saturated, which is confirmed by Figure 13, shown in its respective profile of a longer simulation run in Figure 13a. Additionally, Figure 13b also supports the permeation barrier interpretation, since the BASE Co-Dependent BC after 288 h is still lower than the BASE Coupled BC in the simulation without Pb-Li after only 18 h of evolution (*vide* Figure 6b).

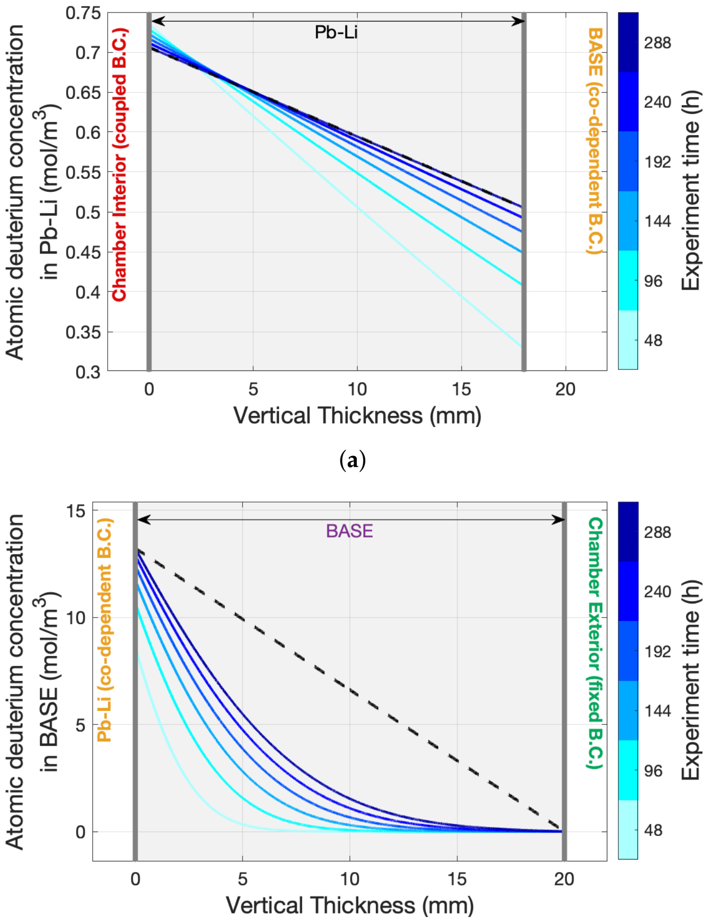

(**a**)

(**b**)

Figure 13. Simulation of concentration profiles evolution during 288 hours in Pb-Li and BASE steel media, using **avg** dissolution parameters (*vide* Tables 1 and 3). Initial gas pressure set at 780 mbar, heater temperature set at 450 °C. (**a**) Concentration profile evolution in Pb-Li. Coupled BC (left) visibly decreases because the continued diffusion eventually reduces the amount of gas available in the UC in meaningful quantities. (**b**) Concentration profile evolution in BASE. Concentration maximum in the order of 13 mol/m^3. Notice how this value is lower than the maximum in Figure 6b, even after a much longer period of system evolution.

5.2. Sensitivity Analysis with Diffusivities and Sieverts' Constants for Pb-Li Taken from Literature

The model of the UC with Pb-Li was then used to perform a sensitivity analysis. This aimed at evaluating the impact of the diffusivity and Sieverts' constant of deuterium in Pb-Li on:

- the time required by the system to reach dissolution equilibrium; and
- the minimum amount of gas to be absorbed by the liquid metal.

For that, dissolution parameters associated with the literature's minimum and maximum $\mathcal{D}_{\mathrm{D}}^{\text{Pb-Li}}$ and $\mathcal{S}_{\mathrm{D}_2}^{\text{Pb-Li}}$ values (at the simulated BASE temperature) were compared to those computed using literature-averaged parameters (minimum and maximum diffusivities and Sieverts' constants were not computed directly using combinations of the extreme values displayed in Table 3 because they result in coefficients that are not representative of the ranges seen in Figure 2).

Using the same geometry from before (*vide* Figure 10), and for a simulation of the BASE temperature set at 450 °C and an initial pressure of 780 mbar, the analysis was done with dissolution parameters derived from:

- Edao-2011 [20] for highest and Shibuya-1987 [10] for lowest diffusivities;
- Aiello-2006 [29] for highest and Feuerstein-1991 [11] for lowest Sieverts' constants.

It should be noted that the diffusivity from the reference Legarda-2010 [18] was neglected due to its large disparity with other curves (*vide* Figure 2a).

Figure 14 displays the evolution of deuterium dissolved in Pb-Li for different scenarios. As expected, the final amount of deuterium dissolved increases significantly with $\mathcal{S}_{\mathrm{D}}^{\text{Pb-Li}}$ and the speed of profile evolution is impacted by $\mathcal{D}_{\mathrm{D}}^{\text{Pb-Li}}$. However, due to the application of the chemical potential continuity principle, the Co-Dependent BC in the Pb-Li side of the interface depends on both the diffusivity and the Sieverts' constant. Thus, scenarios simulated with Edao-2011 and Shibuya-1987 diffusivities do not tend to the same equilibrium conditions.

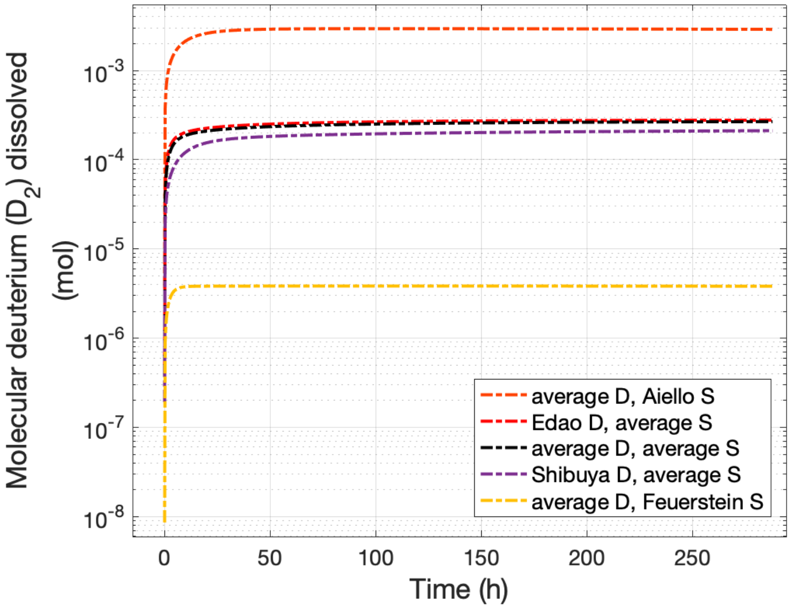

Figure 14. Impact of $\mathcal{D}_{\mathrm{D}}^{\text{Pb-Li}}$ and $\mathcal{S}_{\mathrm{D}}^{\text{Pb-Li}}$ on the amount of deuterium dissolved in Pb-Li. As before, initial gas pressure set to 780 mbar and BASE temperature set to 450 °C. Averages diffusivity and Sieverts' constant obtained using dissolution parameters introduced in Table 3; so curve in *black* is the same as the one presented in Figure 12a. Others are calculated applying dissolution parameters derived from literature [10,11,20,29]. Curves and respective legends displayed in the same descending order; line colors in agreement with Figure 2.

While coupled and Fixed BCs only explicitly depend on the Sieverts' constant (as seen in Figure 4), Equation (7) ensures that Co-Dependent BC will also be dependent on the diffusivities. This implies that, for the computed pressure curves:

- time-related properties do not depend exclusively on the diffusivities; and,
- the relative difference between initial and final pressures does not depend exclusively on the Sieverts' constants.

That is, each curve characteristic is governed by more than one dissolution parameter, in an effective parameter space, and different sets of parameters may lead to indistinguishable characteristics (such as the final pressure). This, and the fact that the typical operation of the UC foresees a finite amount of injected gas, entail that some traditional strategies, such as the time-lag method [14], cannot be used to directly measure dissolution parameters. However, pressure curves simulated with the model bring new insight to VST experiments and, with the strategy presented in Section 4, enable the setup to also measure dissolution parameters, which was not initially planned with this facility. This expands the capabilities of the original VST setup and, moreover, provides a robust method to distinguish sets of dissolution parameters that might lead to similar results in traditional strategies, by comparing the complete experimental and simulated curves.

Table 4 exhibits a quantitative summary of the gas dissolution amounts of the dissolution parameter combinations seen in Figure 14. The last column shows the amounts of deuterium dissolved at the final time step, for simulations ran up to 72 h. Other columns show the amounts of deuterium dissolved in Pb-Li at certain simulation times, but given as fractions of the dissolved amounts at the final time step. In these simulations (for an initial gas pressure of 780 mbar and BASE set temperature of 450 °C), the system is always close to dissolution equilibrium ($^{X}/_{X_f} > 99\%$) after approximately 3 days. For the simulated curves, the most penalizing case (slowest dissolution process to reach 90% of X_f) occurs for a combination of Shibuya-1987 diffusivity and literature-averaged Sieverts' constant.

Table 4. Evolution of gas amount dissolved in Pb-Li (X) at given simulation times (t), for simulations using same parameter combinations as shown in Figure 14. Dissolved gas amounts in middle columns are given in percentages, calculated in relation to gas amounts at final simulation time step (X_f), for simulations up to $t_f = 72\,\text{h}$.

Simulation $\mathcal{D}$	**Simulation $\mathcal{S}$**	**$^{X}/_{X_f}$ (%)**					**X_f (mol)**
avg	Aiello [29]	63.96	90.00	96.74	98.94	99.79	2.94×10^{-3}
Edao [20]	**avg**	73.19	87.78	93.43	96.80	99.10	2.59×10^{-4}
avg	**avg**	71.26	86.88	92.77	96.40	98.97	2.44×10^{-4}
Shibuya [10]	**avg**	55.54	83.50	92.35	96.45	99.00	1.89×10^{-4}
avg	Feuerstein [35]	95.71	99.64	99.82	99.92	99.98	3.84×10^{-6}
$^{t}/_{t_f}$ (%)		10	30	50	17	90	100
Time t (h)		7.2	21.6	36	50.4	64.8	$t_f = 72$

Future experiments with Pb-Li foreseen in the VST setup are planned with an initial procedural step of deuterium dissolution until equilibrium is reached. Simulations ran with the presented model provide crucial indicators to ensure that VST experiments are only started after the system is close to dissolution equilibrium. The versatility of the model allows one to run it in different conditions to match with experiments, in case one wants to vary the temperature or initial pressure during the dissolution phase.

6. Summary and Outlook

A novel modelling approach was proposed and developed to simulate gas dissolution into and diffusion through metals. This was done with the objective of distinguishing between deuterium gas dissolution into/through 316L steel and Pb-Li, since this type of distinction was identified as an issue in static absorption/desorption experiments that attempt to determine the Sieverts' constant of hydrogen isotopes in Pb-Li. This model is considered more accurate than a direct application of Richardson's Permeation Law, since the latter can only be applied to steady-state conditions. In contrast, the developed model is able to estimate the dynamics of gas dissolution through metallic barriers both before and after steady-state conditions are reached.

The implemented model includes a "curve-matching" module. It enables one to determine the dissolution parameters, i.e., the parameters of the Arrhenius functions, for both the diffusivity and Sieverts' constant (solubility) of a gas in a metal. For this, it requires a pressure decrease recorded along time during an experiment using the desired gas-metal pair. This module was used to determine dissolution parameters for deuterium (D_2) in 316L steel using the Upper Chamber (UC) of the Vacuum Sieve Tray (VST) facility. The curve-matching procedure provided these parameters (reported in Table 2), which were coherent and within the ranges for these values reported in literature. Such results validated the model and its approach, which establishes it as a new asset to address the issue of scattered values for the dissolution parameters of hydrogen isotopes in metals (e.g., steel, Pb-Li).

The developed model is also able to take into account interfaces between two metals with different properties. For example, it can be used to simulate a metallic chamber containing a liquid metal. As such, the validated model was subsequently applied to simulate the dissolution of deuterium in the UC containing Pb-Li, as a means of planning for such experiments in the future. This showcases the model's capability to support absorption/desorption experiments, by distinguishing pressure decreases due to dissolution in Pb-Li from losses into/through steel, which are usually neglected.

Two improvements were identified to increase model precision. The first one would consist of taking into account the time required to perform the gas injection in the UC. Since the model assumes instantaneous injection, the gas that already dissolves into the metals during the few seconds of injection is not accounted for. The second one would consist of refining the geometrical simplification of the UC by simulating (an) additional channel(s) to represent fittings. Since they exhibit thinner steel thickness, the small diffusion losses through them could not be estimated by simply increasing each chamber part by a proportional surface area and the total chamber volume by a respective proportional amount. Since the curve-matching procedure warrants a least-squares deviation between simulated and experimental curves, both improvements could address a small overestimation of the diffusivity and Sieverts' constant, that is expected as compensation for unaccounted gas absorption.

Simulations of systems containing Pb-Li presented in this work show the substantial effect that the values of diffusivity and Sieverts' constant have over the amount of hydrogen expected in this metal over time. As such, it can be seen how these coefficients can strongly influence the feasibility of BB concepts based on this metal. The new approach introduced here shows promising capabilities to tackle this issue, when coupled with future experiments in the VST facility. One future study could expand the sensitivity analysis to assess the required pressure sensors accuracy that enables for a more precise measurement of the Sieverts' constant of hydrogen isotopes in Pb-Li, when using static absorption/desorption experiments in the VST. Another could apply the dissolution parameters for deuterium in steel measured in this work to simulations of the UC including Pb-Li, which could then be compared to experimental curves using the curve-matching procedure to measure the dissolution parameters for deuterium in Pb-Li.

Author Contributions: Conceptualization T.P.L., E.D.-A., L.F.; methodology T.P.L.; software T.P.L.; validation T.P.L.; analysis T.P.L.; investigation T.P.L., E.D.-A.; resources E.D.-A.; curation T.P.L.; draft T.P.L.; review T.P.L., E.D.-A., L.F.; visualization T.P.L.; supervision L.F.; project L.F.; funding L.F. All authors have read and agreed to the published version of the manuscript.

Funding: This work has been carried out within the framework of the EUROfusion Consortium and has received funding from the Euratom research and training programme 2014–2018 and 2019–2020 under grant agreement No. 633053. The views and opinions expressed herein do not necessarily reflect those of the European Commission.

Institutional Review Board Statement: Not applicable.

Informed Consent Statement: Not applicable.

Data Availability Statement: Not applicable.

Acknowledgments: The authors would like to thank Niek Lopes Cardozo for his inputs during the preparation of the original thesis that lead to this work [46], and for his comments during the production of this article. The main author is also grateful to the institution FuseNet, for providing him with a student scholarship that partially funded expenses during the initial part of this project.

Conflicts of Interest: The authors declare no conflict of interest. The funders had no role in the design of the study; in the collection, analyses, or interpretation of data; in the writing of the manuscript, or in the decision to publish the results.

Abbreviations & Notation

The following abbreviations and notation are used in this work:

EU-DEMO	European Demonstration Power Plant
FPP	Fusion Power Plant
BB	Breeding Blanket
NMM	Neutron Multiplier Material
Pb-Li	Liquid Lead-Lithium in eutectic proportions
R&D	Research & Development
WCLL	Water-Cooled Liquid-Lithium
VST	Vacuum Sieve Tray (facility)
TLK	Tritium Laboratory Karlsruhe
$\mathcal{D}_X^M$	Diffusivity of atom X in metal M
$\mathcal{S}_{X_2}^M$	Sieverts' constant of gas X_2 in metal M
M	Metal
X_2	Diatomic gas
c_X	Concentration of atom X in a medium
c_X^*	Sieverts' concentration (*vide* Figure 4)
Q_2	Isotopologue of hydrogen molecule
D_2	Deuterium molecule
BC	Boundary Condition
UC	Upper Chamber (of the VST setup)

References

1. Federici, G.; Boccaccini, L.; Cismondi, F.; Gasparotto, M.; Poitevin, Y.; Ricapito, I. An overview of the EU breeding blanket design strategy as an integral part of the DEMO design effort. *Fusion Eng. Des.* **2019**, *141*, 30–42. [CrossRef]
2. Kovari, M.; Coleman, M.; Cristescu, I.; Smith, R. Tritium resources available for fusion reactors. *Nucl. Fusion* **2018**, *58*, 026010. [CrossRef]
3. EUROfusion. *European Research Roadmap to the Realisation of Fusion Energy*; Vol. LONG VERSION, EUROfusion; Programme Management Unit: Garching, Germany, 2018. Available online: www.euro-fusion.org/eurofusion/roadmap (accessed on 19 February 2022).
4. Boccaccini, L.; Aiello, G.; Aubert, J.; Bachmann, C.; Barrett, T.; Del Nevo, A.; Demange, D.; Forest, L.; Hernandez, F.; Norajitra, P.; et al. Objectives and status of EUROfusion DEMO blanket studies. *Fusion Eng. Des.* **2016**, *109–111*, 1199–1206. [CrossRef]
5. Taylor, N.; Ciattaglia, S.; Boyer, H.; Coombs, D.; Jin, X.Z.; Liger, K.; Mora, J.C.; Mazzini, G.; Pinna, T.; Urbonavičius, E. Resolving safety issues for a demonstration fusion power plant. *Fusion Eng. Des.* **2017**, *124*, 1177–1180. [CrossRef]
6. Utili, M.; Ciampichetti, A.; Aiello, A.; Ricapito, I.; Agostini, P.; Desideri, F.; Liger, K. Design of a multipurpose laboratory scale apparatus for the investigation of hydrogen isotopes in PbLi and permeation technologies. *Fusion Eng. Des.* **2012**, *87*, 1342–1346. [CrossRef]
7. Austin Chang, Y.; Fitzner, K.; Zhang, M.X. The solubility of gases in liquid metals and alloys. *Prog. Mater. Sci.* **1988**, *32*, 97–259. [CrossRef]
8. Diaz-Alvarez, E.; Frances, L. Accuracy evaluation and experimental plan of the Multi-Nozzle Vacuum Sieve Tray facility at the Tritium Laboratory Karlsruhe. *Fusion Eng. Des.* **2019**, *146*, 1954–1958. [CrossRef]
9. Polcaro, A.; Ricci, P.; Viola, A. The kinetics of hydrogen absorption in molten Pb/Li alloy. *J. Nucl. Mater.* **1983**, *119*, 291–295. [CrossRef]

10. Shibuya, Y.; Aida, M.; Fujii, Y.; Okamoto, M. Isothermal release of tritium from neutron-irradiated Li17Pb83. *J. Nucl. Mater.* **1987**, *150*, 286–291. [CrossRef]
11. Feuerstein, H.; Gräbner, H.; Horn, S.; Oschinski, J. Behavior of deuterium and rare gases in thermal convection loops with molten Pb-17Li. *Fusion Eng. Des.* **1991**, *14*, 261–271. [CrossRef]
12. Forcey, K.; Ross, D.; Simpson, J.; Evans, D. Hydrogen transport and solubility in 316L and 1.4914 steels for fusion reactor applications. *J. Nucl. Mater.* **1988**, *160*, 117–124. [CrossRef]
13. Viola, A.; Pierini, G.; Lolli-Ceroni, P.; Douglas, K. Kinetics of deuterium desorption from Pb-17Li eutectic. *Fusion Eng. Des.* **1991**, *14*, 249–260. [CrossRef]
14. Xiukui, S.; Jian, X.; Yiyi, L. Hydrogen permeation behaviour in austenitic stainless steels. *Mater. Sci. Eng. A* **1989**, *114*, 179–187. [CrossRef]
15. Kaufman, M. *Principles of Thermodynamics*; Number 15 in Undergraduate Chemistry; Marcel Dekker: New York, NY, USA, 2002.
16. Çengel, Y.A.; Boles, M.A. *Thermodynamics: An Engineering Approach*, 5th ed.; McGraw-Hill Series in Mechanical Engineering; McGraw-Hill Higher Education: Boston, MA, USA, 2006.
17. Mas de les Valls, E.; Sedano, L.; Batet, L.; Ricapito, I.; Aiello, A.; Gastaldi, O.; Gabriel, F. Lead–lithium eutectic material database for nuclear fusion technology. *J. Nucl. Mater.* **2008**, *376*, 353–357. [CrossRef]
18. Legarda, F.; Alberro, G.; Peñalva, I.; Sarrionandia-Ibarra, A.; Esteban, G.A. *Experimental Determination of Reference Sieverts' Constant and Diffusivity Values for Tritium in LiPb*; Technical Report TW6-TTBC-005; EFDA: Bilbao, Spain, 2010.
19. Okamoto, M.; Shibuya, Y.; Aida, M.; Fujii, Y. Tritium recovery from neutron irradiated li-pb alloys. *Fusion Eng. Des.* **1989**, *8*, 345–348. [CrossRef]
20. Edao, Y.; Noguchi, H.; Fukada, S. Experiments of hydrogen isotope permeation, diffusion and dissolution in Li–Pb. *J. Nucl. Mater.* **2011**, *417*, 723–726. [CrossRef]
21. Terai, T.; Nagai, S.; Yoneoka, T.; Takahashi, Y. Diffusion coefficient of tritium in molten lithium-lead alloy (Li17Pb83) under neutron irradiation at elevated temperatures. *J. Nucl. Mater.* **1992**, *187*, 247–253. [CrossRef]
22. Reiter, F. Solubility and diffusivity of hydrogen isotopes in liquid Pb-17Li. *Fusion Eng. Des.* **1991**, *14*, 207–211. [CrossRef]
23. Okitsu, H.; Edao, Y.; Okada, M.; Fukada, S. Analysis of diffusion and dissolution of two-component hydrogen (H+D) in lead lithium. *Fusion Eng. Des.* **2012**, *87*, 1324–1328. [CrossRef]
24. Fauvet, P.; Sannier, J. Hydrogen behaviour in liquid 17Li83Pb alloy. *J. Nucl. Mater.* **1988**, *155–157*, 516–519. [CrossRef]
25. Sze, D.K.; Clemmer, R.; Cheng, E.T. *LiPb, a Novel Material for Fusion Applications*; Technical Report UWFDM-378; Fusion Technology Institute, University of Wisconsin: Madison, WI, USA, 1980.
26. Fukada, S.; Edao, Y. Unsolved issues on tritium mass transfer in Li–Pb liquid blankets. *J. Nucl. Mater.* **2011**, *417*, 727–730. [CrossRef]
27. Katsuta, H.; Iwamoto, H.; Ohno, H. Hydrogen solubility in liquid Li17Pb83. *J. Nucl. Mater.* **1985**, *133–134*, 167–170. [CrossRef]
28. Wu, C.H.; Blair, A.J. A study of the interaction of tritium with liquid Li17Pb83. In Proceedings of the 12. Symposium Held in Juelich, Juelich, Germany, 13–17 September 1983; Volume 1, pp. 699–704. [CrossRef]
29. Aiello, A.; Ciampichetti, A.; Benamati, G. Determination of hydrogen solubility in lead lithium using sole device. *Fusion Eng. Des.* **2006**, *81*, 639–644. [CrossRef]
30. Wu, C.H. The Solubility of Deuterium in Lithium-Lead Alloys. *J. Nucl. Mater.* **1983**, *114*, 30–33. [CrossRef]
31. Wu, C. The interaction of hydrogen isotopes with lithium-lead alloys. *J. Nucl. Mater.* **1984**, *123*, 941–945. [CrossRef]
32. Chan, Y.C.; Veleckis, E. A Thermodynamic Investigation of Dilute Solutions of Hydrogen in Liquid Li-Pb Alloys. *J. Nucl. Mater.* **1984**, *123*, 935–940. [CrossRef]
33. Hoch, M. The solubility of hydrogen, deuterium and tritium in liquid lead-lithium alloys. *J. Nucl. Mater.* **1984**, *120*, 102–112. [CrossRef]
34. Malara, C.; Casini, G.; Viola, A. Analysis of tritium behaviour and recovery from a water-cooled Pb17Li blanket. *Fusion Eng. Des.* **1995**, *28*, 299–312. [CrossRef]
35. Feuerstein, H.; Gräbner, H.; Horn, S.; Oschinski, J. Transport of deuterium and rare gases by flowing molten Pb-17Li. *J. Nucl. Mater.* **1991**, *179–181*, 882–885. [CrossRef]
36. Barrer, R.M. *Diffusion in and through Solids*; The Cambridge Series of Physical Chemistry; Cambridge University Press: Cambridge, UK, 1941. ISBN10: 5-88379-533-1.
37. Fowler, R.H.; Smithells, C.J. A theoretical formula for the solubility of hydrogen in metals. *Proc. R. Soc. Lond. Ser. A Math. Phys. Sci.* **1937**, *160*, 37–47. [CrossRef]
38. Lacher, J.R. A theoretical formula for the solubility of hydrogen in palladium. *Proc. R. Soc. Lond. Ser. A Math. Phys. Sci.* **1937**, *161*, 525–545. [CrossRef]
39. Crank, J. *The Mathematics of Diffusion*, 2nd ed.; Clarendon Press: Oxford, UK, 1975.
40. Peiró, J.; Sherwin, S. Finite Difference, Finite Element and Finite Volume Methods for Partial Differential Equations. In *Handbook of Materials Modeling: Methods*; Yip, S., Ed.; Springer: Dordrecht, The Netherlands, 2005; pp. 2415–2446. [CrossRef]
41. Schäfer, M. *Computational Engineering—Introduction to Numerical Methods*; Springer: Berlin/Heidelberg, Germany, 2006.
42. Auer, P.L.; Murbach, E.W. Diffusion across an Interface. *J. Chem. Phys.* **1954**, *22*, 1054–1059. [CrossRef]
43. Dean, J.A.; Lange, N.A. (Eds.) *Lange's Handbook of Chemistry*, 15th ed.; McGraw-Hill Handbooks, McGraw-Hill: New York, NY, USA, 1999; ISBN 978-0-07-016384-3.

44. Kishimoto, N.; Tanabe, T.; Suzuki, T.; Yoshida, H. Hydrogen diffusion and solution at high temperatures in 316L stainless steel and nickel-base heat-resistant alloys. *J. Nucl. Mater.* **1985**, *127*, 1–9. [CrossRef]
45. Lee, S.K.; Kim, H.S.; Noh, S.J.; Han, J.H. Hydrogen Permeability, Diffusivity, and Solubility of SUS 316L Stainless Steel in the Temperature Range 400 to 800 OC for Fusion Reactor Applications. *J. Korean Phys. Soc.* **2011**, *59*, 3019–3023. [CrossRef]
46. Pomella Lobo, T. A Quasi-2D Model to Simulate Thermodynamics and Kinetics of Hydrogen Isotopes Dissolution in Pb-Li and Steel. Master's Thesis, Eindhoven University of Technology, Eindhoven, The Netherlands, 2018.